Near Surface Geophysics, 2017, **15**, 187-199 doi: 10.3997/1873-0604.2016050

Reconstruction quality of SIP parameters in multi-frequency complex resistivity imaging

Maximilian Weigand[1*], Adrián Flores Orozco[2] and Andreas Kemna[1]

[1]*Department of Geophysics, University of Bonn, Meckenheimer Allee 176, 53115 Bonn, Germany*
[2]*Institute of Geodesy and Geophysics, TU-Wien, Gusshausstrasse 27/29, 1040 Vienna, Austria*

Received April 2016, revision accepted November 2016

ABSTRACT

Complex resistivity imaging provides information on the subsurface distribution of the electrical conduction and polarisation properties. Spectral induced polarisation (SIP) refers to the frequency dependence of these complex resistivity values. Measured SIP signatures are commonly analysed by performing a Cole–Cole model fit or a Debye decomposition, yielding in particular chargeability and relaxation time values. Given the close relation of these parameters with petrophysical properties of relevance in various hydrogeological and environmental applications, it is crucial to understand how well they can be reconstructed from multi-frequency complex resistivity imaging with subsequent Cole–Cole or Debye decomposition analysis. In this work, we investigate, in a series of numerical simulations, the reconstruction behaviour of the main spectral induced polarisation parameters across a two-dimensional complex resistivity imaging plane by considering a local anomalous polarisable body at different depths. The different anomaly positions correspond to different cumulated sensitivity (coverage) values, which we find to be a simple and computationally inexpensive proxy for resolution. Our results show that, for single-frequency measurements, the reconstruction quality of resistivity and phase decreases strongly with decreasing cumulated sensitivity. A similar behaviour is found for the recovery of Cole–Cole and Debye decomposition chargeabilities from multi-frequency imaging results, while the reconstruction of the Cole–Cole exponent shows non-uniform dependence over the examined sensitivity range. In contrast, the Cole–Cole and Debye decomposition relaxation times are relatively well recovered over a broad sensitivity range. Our results suggest that a quantitative interpretation of petrophysical properties derived from Cole–Cole or Debye decomposition relaxation times is possible in an imaging framework, while any parameter estimate derived from Cole–Cole or Debye decomposition chargeabilities must be used with caution. These findings are of great importance for a successful quantitative application of spectral induced polarisation imaging for improved subsurface characterisation, which is of interest particularly in the fields of hydrogeophysics and biogeophysics.

INTRODUCTION

The induced polarisation (IP) method yields images of the complex resistivity (CR) of the subsurface, which provides information on the conduction and polarisation properties of the measured soils or rocks. The measurements can be performed at different frequencies (typically below 10 kHz), in the so-called spectral IP (SIP) method, to obtain information on the frequency dependence of the CR.

Due to its simplicity, the Cole–Cole (CC) model is widely used to describe the SIP response (e.g., Pelton *et al.* 1978; Luo and Zhang 1998). Yet, in recent years, the Debye decomposition (DD) approach has been promoted as a robust and flexible alternative to the CC model in (near-surface) geophysical applications (e.g., Lesmes and Morgan 2001; Nordsiek and Weller 2008; Florsch, Revil and Camerlynck 2014; Weigand and Kemna 2016b).

While initially the IP method has been mainly used for the prospection of ore deposits (e.g., Pelton *et al.* 1978), over the last 15 years, the potential of CR imaging has also been demonstrated for various hydrogeological and environmental applications, including lithological discrimination (e.g., Kemna, Binley and Slater 2004; Mwakanyamale *et al.* 2012), mapping and quantification of hydraulic conductivity (e.g., Kemna *et al.* 2004; Hördt *et al.* 2007), monitoring the integrity and performance of reactive barriers (Slater and Binley 2006), mapping and characterisation of contaminant plumes (e.g., Kemna *et al.* 2004; Flores Orozco *et al.* 2012a), monitoring of sulphide mineral precipitation (e.g., Williams *et al.* 2009; Flores Orozco, Williams and Kemna 2013), and monitoring of micro-particle injection and

* MWEIGAND@GEO.UNI-BONN.DE

propagation (Flores Orozco *et al.* 2015). These field-scale applications have also prompted the development of models describing the link between the CR response and lithologic, textural, hydraulic, or geochemical soil/rock properties (see, e.g., Slater (2007), Kemna *et al.* (2012) and the references therein). The potential of the SIP method has also been demonstrated for applications in the emerging field of biogeophysics (e.g., Atekwana and Slater 2009). Examples of such applications include the detection of alterations at mineral–fluid interfaces due to microbial growth (e.g., Abdel Aal *et al.* 2004) or biostimulated mineral precipitation (e.g., Williams *et al.* 2009; Flores Orozco *et al.* 2011), detection of biofilm formation (e.g., Ntarlagiannis *et al.* 2005; Davis *et al.* 2006), and characterisation of tree roots (e.g., Zanetti *et al.* 2011) or crop roots (Weigand and Kemna 2016a). The variety of these studies demonstrates the growing interest in the application of CR (or SIP) imaging.

It is well known that electrical images are characterised by a spatially variable image resolution (e.g., Oldenburg and Li 1999; Friedel 2003; Binley and Kemna 2005), which needs to be taken into account in the interpretation of the resulting images. Day-Lewis, Singha and Binley (2005) found a spatially variable reconstruction quality of water content determined from electrical resistivity measurements, with an increasing inaccuracy of the inferred water content estimates with decreasing image resolution. This resolution-related phenomenon was referred to by the authors as "correlation loss", as it can be considered as loss of information in the resistivity images due to poor resolution. Kemna (2000) demonstrated that the analysis of the cumulated sensitivity can provide insights into the variable image resolution. Nguyen *et al.* (2009) found, for regions with cumulated sensitivity below some threshold value, an increase in the correlation loss for the mass fraction between fresh water and seawater reconstructed from electrical resistivity imaging results. However, even if the problem of correlation loss has been pointed out for conventional resistivity imaging, it has not yet been addressed for single- or multi-frequency (spectral) IP imaging. The assessment of correlation loss is critical for the desired application of petrophysical models established on the basis of laboratory studies to imaging results obtained in the field.

We here investigate, by means of numerical simulations, the reconstruction quality of CC model and DD parameters recovered from multi-frequency CR images. We consider a standard dipole–dipole surface survey over a homogeneous, non-polarisable half-space containing a 2D polarisable anomaly, whose vertical position is systematically varied to investigate its reconstruction in areas with different sensitivity levels in the inversion. Hereafter, we refer to reconstruction quality as the deviation of the recovered model parameters from their original values. We analyse and compare the reconstruction quality of single- and multi-frequency (spectral) IP parameters as a function of cumulated sensitivity. We also investigate the impact of data noise on the reconstruction quality, considering that data quantification is critical for quantitative IP imaging applications (e.g., Flores Orozco, Kemna and Zimmermann 2012b; Kemna *et al.* 2012).

METHODS

Forward modelling and inversion

Synthetic data, i.e., complex transfer impedances, are computed using the 2.5D finite-element modelling code CRMod (Kemna 2000). CRMod solves the underlying 2.5D forward problem (Helmholtz equation) for a given 2D CR distribution. For details of the implementation, we refer to Kemna (2000). Data noise is added from a normally distributed ensemble of random numbers. To provide comparable results, all simulations are conducted using the same ensemble of random numbers, scaled by previously chosen standard deviations.

The noise-contaminated data are inverted using CRTomo (Kemna 2000), which is a smoothness-constraint, Gauss–

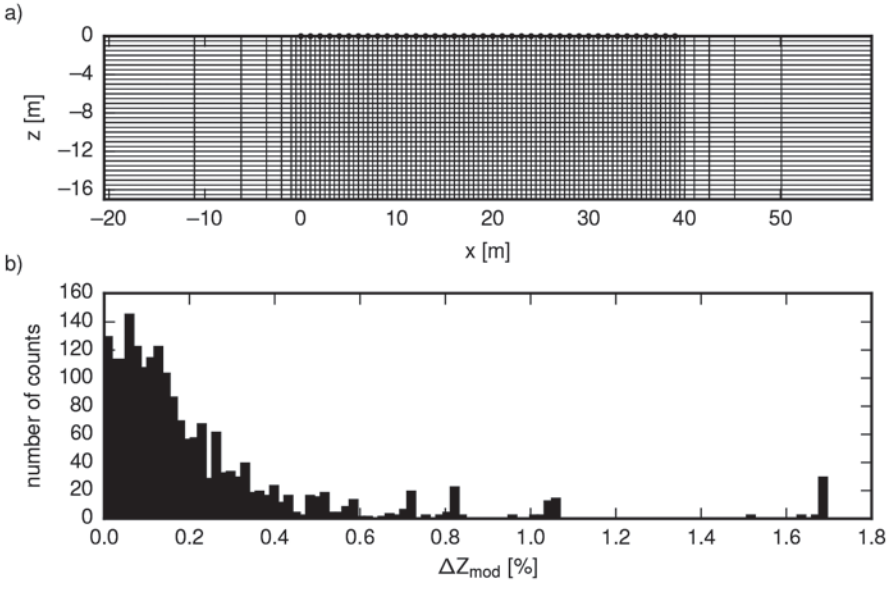

Figure 1 (a) Finite-element grid used for the forward modelling. (b) Distribution of percentage errors of modelled impedance magnitude values ($\mathbf{\Delta} Z_{mod}$) for all used measurement configurations, determined for a homogeneous resistivity model (half-space).

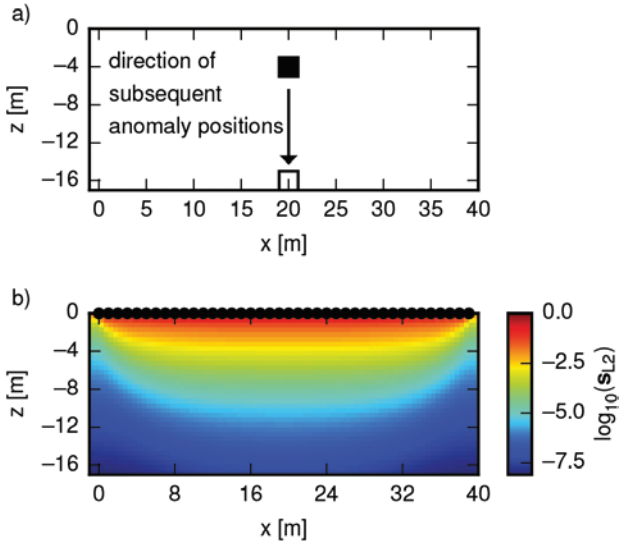

Figure 2 (a) Model used for the numerical simulations and (b) corresponding (L_2-normed) cumulated sensitivity distribution (normalised to 1). The model consists of a homogeneous half-space ($|\rho|$ = 100 Ωm, ϕ = 0 mrad) with an embedded polarisable anomaly (indicated by the black rectangle), the depth position of which is varied in the simulations. The positions of the surface electrodes are indicated by black dots. Outer elements of the modelling grid are not shown (cf. Figure 1a).

Newton-type inversion scheme. The data are weighted in the inversion by individual errors (see Appendix A).

Image appraisal is done using the L_1- and L_2-normed cumulated sensitivity (coverage) and the diagonal entries of the model resolution matrix (see Appendix B). Throughout this study, normalised cumulative, error-weighted sensitivities (hereafter simply referred to as sensitivity) are presented, as they offer better comparability.

Cole–Cole model

The frequency-dependent electrical properties of soils and rocks are often described by the empirical CC model (e.g., Cole and Cole 1941). In terms of CR, $\rho(\omega)$, with angular frequency ω, the CC model can be expressed after Pelton *et al.* (1978) as

$$\rho(\omega) = \rho_0\left(1 - m\left[1 - \frac{1}{1 + (j\omega\tau)^c}\right]\right), \quad (1)$$

where ρ_0 is the DC resistivity (low-frequency asymptote), m is the CC chargeability, τ is the CC relaxation time, c is the CC exponent, and j is the imaginary unit. Parameter ρ_0 defines the amplitude of the magnitude spectrum ($|(\rho(\omega)|$), whereas parameter m determines the amplitude of the phase spectrum ($\phi(\omega)$). Parameter c describes the asymptotic slope of the symmetric phase spectrum (in log–log representation), i.e., the degree of frequency dispersion, and parameter τ is inversely related to the peak frequency of the imaginary part of the resistivity, i.e., $\omega_{\max,\rho}$", by $\omega_{\max,\rho}$" = 1/τ. The values of m and c range from 0 to 1, whereas τ values may span several orders of magnitude (e.g., Pelton *et al.* 1978; Vanhala 1997; Luo and Zhang 1998).

Debye decomposition

The DD scheme describes the CR spectrum using a superposition of a large number of Debye polarisation terms (e.g., Nordsiek and Weller 2008):

$$\rho(\omega) = \rho_{0,\mathrm{DD}}\left(1 - \sum_{k=1}^{N} m_k\left[1 - \frac{1}{1 + j\omega\tau_k}\right]\right), \quad (2)$$

where N is the number of relaxation times (i.e., Debye polarisation terms) used for the superposition, m_k is the kth chargeability corresponding to the kth relaxation time τ_k, and $\rho_{0,\mathrm{DD}}$ is the DC resistivity (as obtained from the DD). The relaxation times are chosen to cover the frequency range spanned by the data according to the inverse relationship $\tau = 1/\omega_{\max,\rho}$" (e.g., Weigand and Kemna 2016b). For each frequency decade, 20 relaxation times are used, and the relaxation time range is extended by two orders of magnitude at each end of the covered frequency range, as suggested by Weigand and Kemna (2016b,c).

The resulting distribution of relaxation times $mk(\tau k)$ is called the relaxation time distribution, from which parameters similar to the CC parameters are derived:

- The *total chargeability*, $m_{\mathrm{tot}} = \sum_{k=1}^{N} m_k$, provides an analog to the CC chargeability m. However, m_{tot} only accounts for polarisation contributions within the data frequency range due to the much narrower spectral shape of the Debye response compared with typical CC responses (with $c < 1$).
- The *mean logarithmic relaxation time*, τ_{mean}, denotes the chargeability-weighted logarithmic mean value of the DD relaxation times (Nordsiek and Weller 2008):

$$\tau_{\mathrm{mean}} = \exp\left(\frac{\sum_{k=1}^{N} m_k \log(\tau_k)}{\sum_{k=1}^{N} m_k}\right).$$

DESIGN OF NUMERICAL EXPERIMENTS

The numerical experiments are conducted on a model domain of 80 m × 17 m (as depicted in Figure 1a), with the underlying finite-element mesh consisting of 3128 rectangular cells, each composed of four triangular elements. Forty electrodes are located at the surface with an equidistant spacing of 1 m. Only the quadratic finite-element cells below the electrodes are used for the analysis, and they are equally sized with an edge length of 0.5 m. To increase modelling accuracy, additional elements with an exponentially increasing width are used at both sides of the grid. Simulations are performed using a dipole–dipole measurement scheme composed of skip-0,1,2,3 configurations, resulting in 1944 measurements. The "skip-number" refers to the dipole length, indicating the number of electrodes "skipped" between the two current electrodes and the two voltage electrodes, respectively.

For instance, the skip-0 configuration uses adjacent electrodes for current injection and voltage measurement. Resistance (impedance magnitude) modelling errors for a homogeneous half-space lie below 2% for all measurement configurations (Figure 1b).

The surface electrode configuration used in this study exhibits a cumulative sensitivity distribution that decreases monotonically with depth (Figure 2b). Thus, an anomaly placed at different depths in the subsurface (Figure 2a) is associated with different cumulative sensitivity levels. The CR model used to compute synthetic data is defined as a homogeneous background ($|\rho| = 100$ Ωm, $\phi = 0$ mrad) containing an anomalous body (4 × 4 model cells, corresponding to a size of 2 m × 2 m) with varying resistivity magnitude and phase values. Since the spatial extension of the anomaly is relatively small (given the modelling domain and the used measurement configurations) and since anomalous resistivity magnitude values were only varied within one order of magnitude relative to the background value, the current density (and sensitivity) distributions do not differ significantly from the distribution for a homogeneous model. Therefore, we use the sensitivity values of the homogeneous model in the analysis of the reconstruction quality of the CC parameters for models containing the polarisable anomaly. However, the diagonal entries of the model resolution matrix, i.e., $\underline{\underline{R}}$ (see Appendix B), are computed after the final iteration of the inversion process. As the final values of the regularisation parameter λ differ for the different anomaly locations, so do the computed diagonal entries of $\underline{\underline{R}}$ vary on this account (cf. equation (10)). Although this makes a quantitative comparison for the different anomaly locations difficult, the diagonal entries of $\underline{\underline{R}}$ are presented in the following sections to show their general behaviour in comparison with cumulated sensitivity.

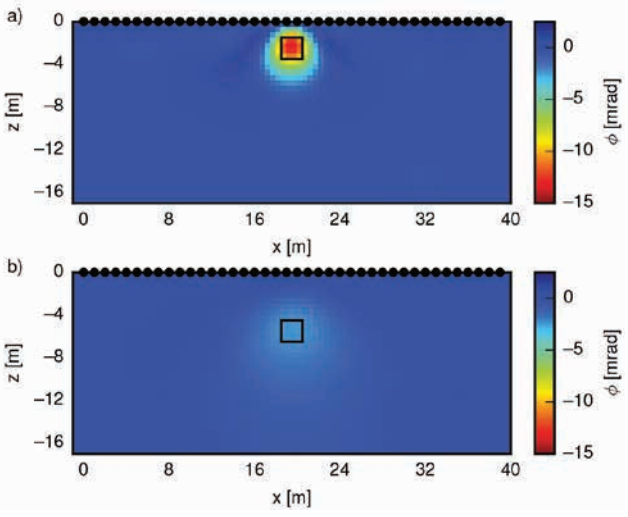

Figure 3 Resistivity phase imaging results for the model shown in Figure 2a for two different depths of the polarisable (–30 mrad) anomaly. The position of the anomaly is marked by the black rectangle.

Single-frequency reconstruction

In a first step, we investigate the reconstruction quality of resistivity magnitude and phase values in the region of the anomaly, i.e., the deviation between original and recovered values, for a single-frequency data set. In the single-frequency studies, we investigate three scenarios: (i) 10 Ωm, –30 mrad (conductive, polarisable anomaly); (ii) 100 Ωm, –30 mrad (polarisable anomaly); and (iii) 1000 Ωm, –30 mrad (resistive, polarisable anomaly). Figure 3 shows exemplary inversion results for the second scenario for two depths of the anomaly.

A small, stabilising noise component of 0.1% Gaussian noise is added to the impedance magnitude data, and Gaussian noise with a standard deviation of 0.5 mrad is added to the impedance phase data. The error estimate in the inversion assumes 3% relative and 0.001 Ω absolute error for the impedance magnitude (resistance) and 1% relative and 0.5-mrad absolute error for the impedance phase.

The inverted resistivity magnitude and phase values of the anomaly pixels (i.e., model cells within the anomaly region) are averaged (arithmetic mean of log magnitude and phase, respectively), and the deviations from the original values are calculated as a measure of reconstruction quality. These deviations are analysed against the averaged (arithmetic mean of log values) cumulative sensitivity values ($\underline{s}_{L1}$ and $\underline{s}_{L2}$), as well as against the diagonal entries of the model resolution matrix (diag($\underline{\underline{R}}$)), for the different anomaly locations.

Multi-frequency reconstruction

The next step in our study is to examine the reconstruction quality of the CC model parameters inferred from multi-frequency imaging results. The original CC parameters of the anomaly are chosen

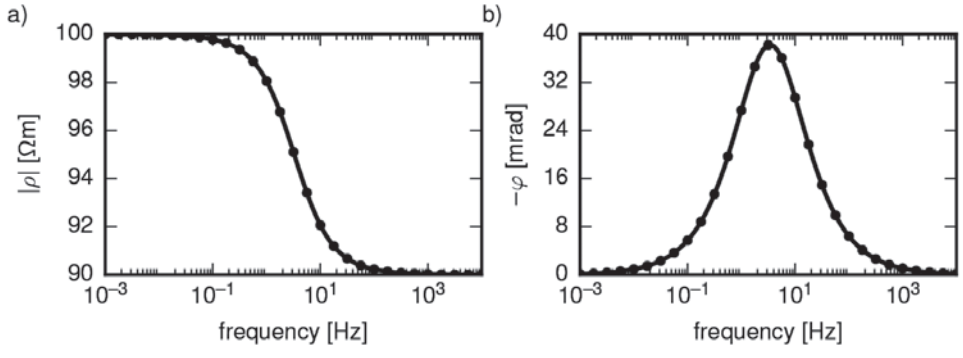

Figure 4 (a) CR magnitude and (b) phase CC model response of the polarisable anomaly simulated in this study (for CC parameters: ρ_0 = 100 Ωm, m = 0.1, τ = 0.049 s, c = 0.8). The dots indicate the considered measurement frequencies.

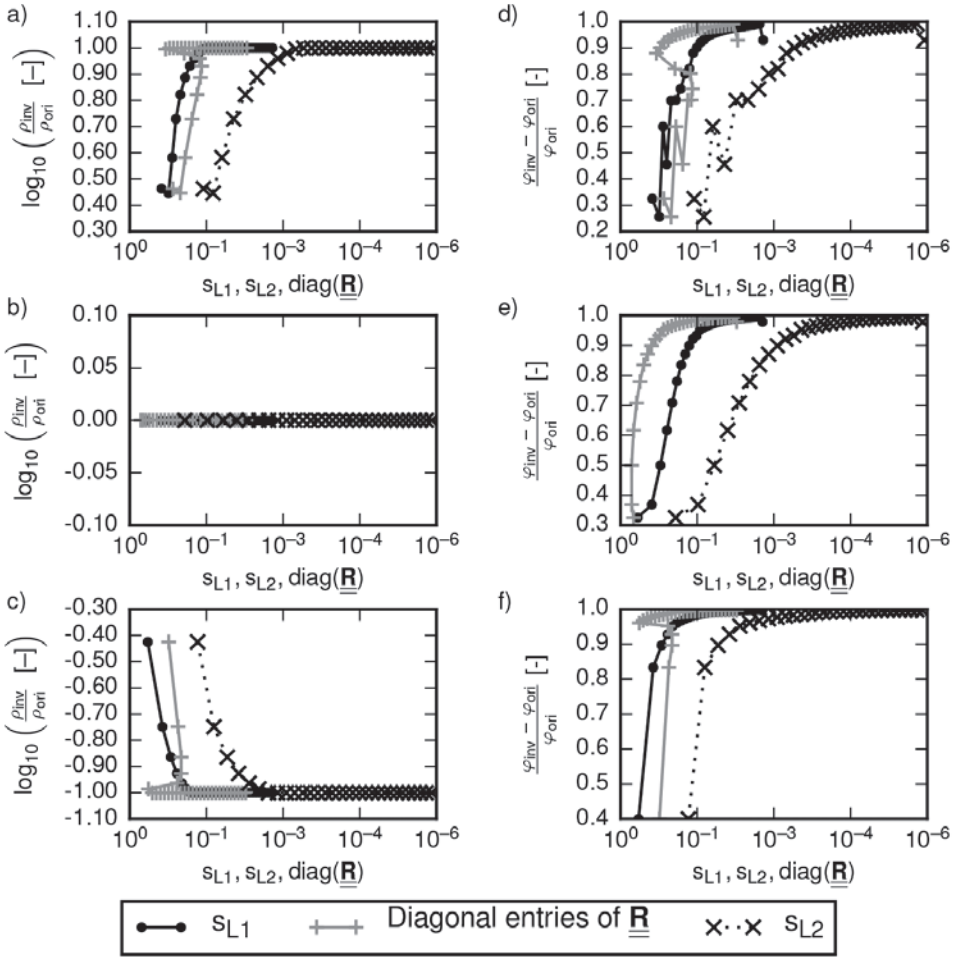

Figure 5 Deviation between recovered and original resistivity (a, b, and c) magnitude and (d, e, and f) phase values in the anomaly region. Results are presented for different depth positions of the anomaly (indicated by the markers along each curve), plotted as a function of L_1 cumulated sensitivity (s_{L1}), L_2 cumulated sensitivity (s_{L2}), and resolution (i.e., diagonal entry of the model resolution matrix) in the anomaly region. Results are shown for three scenarios: (a and d) a conductive, polarisable anomaly (model values 10 Ωm, –30 mrad); (b and e) a solely polarisable anomaly (model values 100 Ω, –30 mrad) (cf. Figure 3); and (c and f) a resistive, polarisable anomaly (model values 1000 Ωm, –30 mrad), each embedded in a homogeneous background (model values 100 Ωm, 0 mrad). The reconstructed values are extracted from the corresponding (single-frequency) CR imaging results and averaged over the 16 model cells that comprise the anomaly. A phase noise level of 0.5 mrad is assumed in the inversion.

as $\rho_0 = 100$ Ωm, $m = 0.1$, $\tau = 0.049$ s , and $c = 0.8$, so that the peak of the phase response occurs in the center of the considered frequency range (at approximately 3 Hz). Based on these parameters, impedance measurements at 29 frequencies between 10^{-3} Hz and 10^{4} Hz (equally spaced on a logarithmic scale) are numerically computed, as illustrated in Figure 4. The model background is set to 100 Ωm and 0 mrad for all frequencies. CR models are created for each of the 29 frequencies and used to model synthetic datasets, which are then independently inverted. Following this, a CC model is fitted to the CR spectra extracted from the multi-frequency images for each of the anomaly pixels (hereafter referred to as intrinsic spectra). Likewise, the DD is applied to the obtained intrinsic spectra. In the final step, the arithmetic mean values of the resultant spectral model parameters ($\log(\rho_0)$, m, $\log(\tau)$, m_{tot}, $\log(\tau_{mean})$ are computed. Thus, for each vertical anomaly position, one set of averaged spectral model parameters is obtained.

To assess the reconstruction quality, the deviations between the recovered and original values are analysed against the $\underline{s}_{L1}$, $\underline{s}_{L2}$, and $\mathrm{diag}(\underline{\underline{R}})$ values, averaged (arithmetic mean of log values) over the anomaly pixels. The following parameters denote the percentage deviation of the recovered parameters from the original CC parameters, representing a measure of reconstruction quality:

$$\eta_m = \frac{m_{orig} - m}{m_{orig}} \cdot 100, \tag{3}$$

$$\eta_{mtot} = \frac{m_{orig} - m_{tot}}{m_{orig}} \cdot 100, \tag{4}$$

$$\eta_\tau = \frac{\tau_{orig} - \tau}{\tau_{orig}} \cdot 100, \tag{5}$$

$$\eta_{\tau,mean} = \frac{\tau_{orig} - \tau_{mean}}{\tau_{orig}} \cdot 100, \tag{6}$$

$$\eta_c = \frac{c_{orig} - c}{c_{orig}} \cdot 100, \tag{7}$$

with the subscript "orig" denoting the original CC parameters used to generate the CR response in the forward model. The

other parameters are recovered from the CC fit and the DD of the imaging results.

A stabilising noise component of 0.1% Gaussian noise is added to the impedance magnitude data, and an impedance magnitude (resistance) error estimate comprising 3% relative error and 0.001 Ω absolute error is used in the inversions to account for numerical errors in the forward solution. Gaussian noise of different levels (0.05, 0.1, and 0.5 mrad) is added to the impedance phase datasets to investigate the effects of data noise and error estimation on the reconstruction of the CC and DD parameters. Here, at first, phase error estimates equal to the actual noise level in the phase data are assumed in the inversion, thus adequately accounting for the added noise. In subsequent inversions, the actual phase noise level is deliberately underestimated by up to one order of magnitude to investigate the effect of overfitting on the reconstruction quality.

In a final numerical simulation, we investigate the quality of reconstructed τ and τ_{mean} values for different degrees of frequency dispersion (i.e., different c values) and different spectral positions of the phase peak (i.e., different τ values) in the original CC model response of the anomaly.

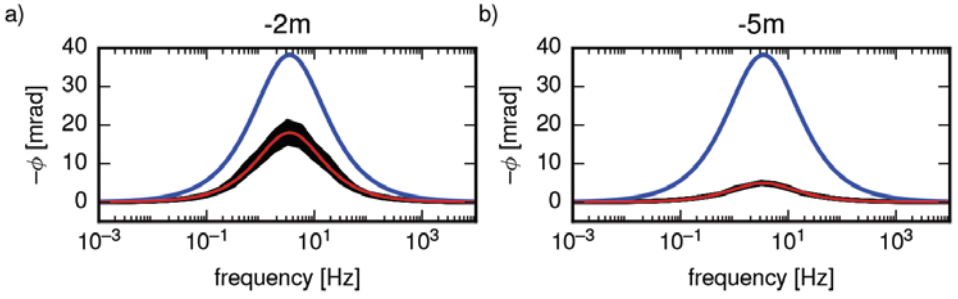

Figure 6 Recovered phase values for all 16 elements (black lines), the corresponding original spectral response (blue curve), and the response of the fitted CC model (red curve) in the anomaly region for (a) a 2-m depth and (b) a 5-m depth of the anomaly (referring to the top boundary of the anomaly) (cf. Figure 3).

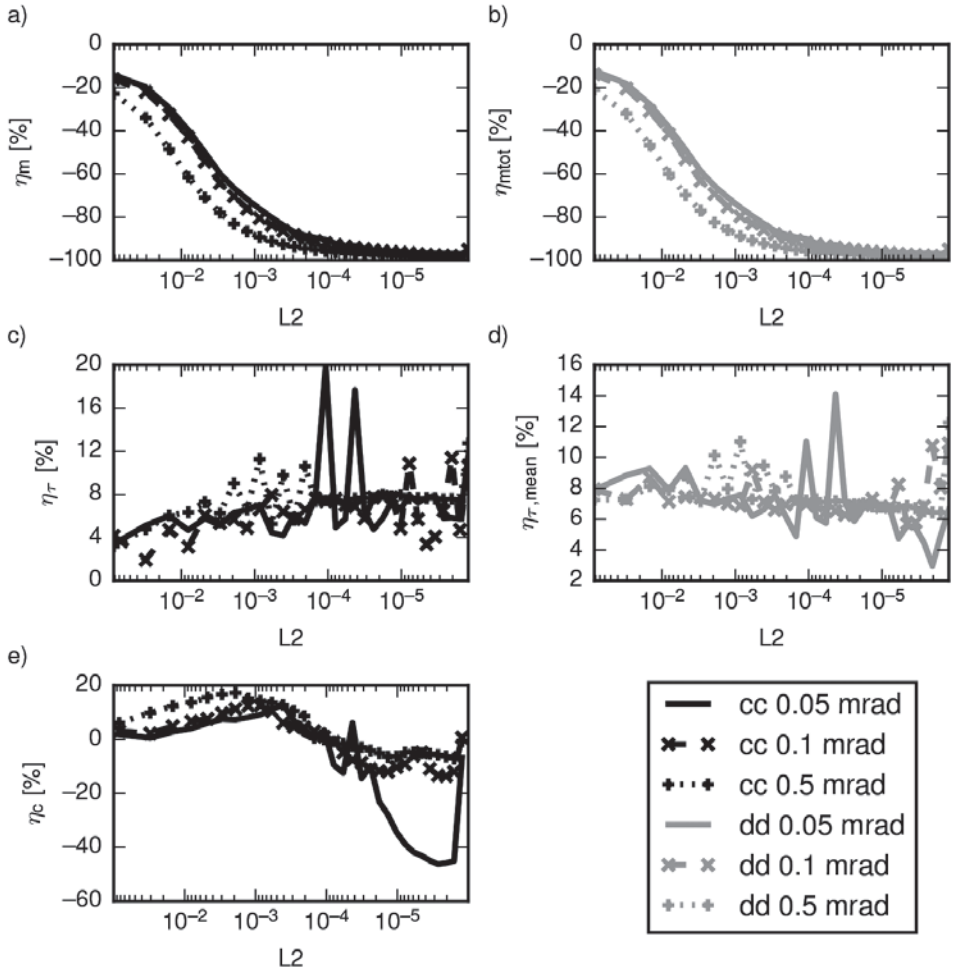

Figure 7 Reconstruction quality parameters for the recovered CC and DD parameters of the anomaly pixels plotted against decreasing sensitivity values (L_2), i.e., increasing depth locations of the anomaly. (a) η_m, (b) η_{mtot}, (c) η_τ, (d) $\eta_{\tau,mean}$, (e) η_c. Simulations were performed for a phase data noise level of 0.05, 0.1, and 0.5 mrad, respectively. The phase error estimate in the inversions was chosen accordingly.

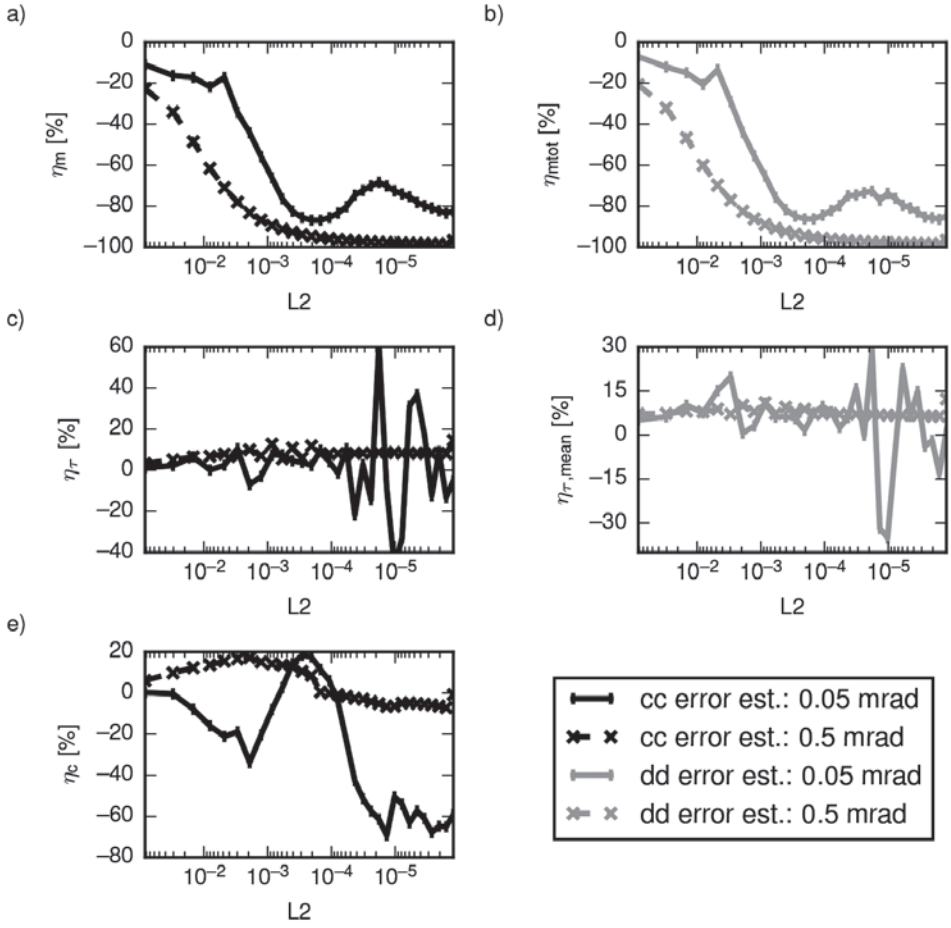

Figure 8 Reconstruction quality parameters for the recovered CC and DD parameters of the anomaly pixels plotted against decreasing sensitivity values (L_2), i.e., increasing depth locations of the anomaly. (a) η_m, (b) η_{mtot}, (c) η_τ, (d) $\eta_{\tau,mean}$, (e) η_c. Results are averaged over the 16 pixels of the anomaly. Simulations were performed for a phase data noise level of 0.5 mrad and two different phase error estimates used in the inversions, corresponding to an underestimation of noise (0.05-mrad error) and the correct estimation of noise (0.5-mrad error).

RESULTS

Single-frequency results

The reconstruction quality of resistivity magnitude decreases with decreasing sensitivity for anomalies with a contrasting magnitude value, compared with the background magnitude (Figure 5a,c). The contrast between anomaly and background values, i.e., whether the anomaly is conductive or resistive, determines the sign of the deviation, for over- or underestimated values. If no contrast is present in the magnitude, reconstruction quality is independent of sensitivity (Figure 5b). The phase reconstruction curves do not show such dependence on the magnitude contrast (Figure 5d–f). The three cases, referring to the same value of the phase anomaly ($\phi = -30$ mrad), reveal a monotonic decrease in reconstruction quality with decreasing sensitivity (s_{L1}, s_{L2}) and resolution (diag($\underline{\underline{R}}$)) values. Reconstruction quality curves in Figure 5 also reveal a slightly different behaviour depending on whether the anomaly is conductive or resistive. In particular, for the same depth position of the anomaly, a smaller deviation of the reconstructed phase values is observed in case of a conductive anomaly (Figure 5d) in comparison to a resistive anomaly (Figure 5f). This indicates an improved phase reconstruction capability in conductive regions, where current flow is focused. Furthermore, Figure 5 reveals a similar qualitative behaviour with respect to sensitivity (for both L_1 and L_2 curves) and resolution (diag($\underline{\underline{R}}$)), demonstrating that (cumulated) sensitivity is an adequate proxy to evaluate image resolution.

Multi-frequency results

Figure 6 shows the recovered spectral phase response for the anomaly located at 2- and 5-m depths, respectively, and thus associated with different sensitivity (resolution) levels. Both reconstructed spectra exhibit an underestimation of the absolute phase values in comparison with the original values. This underestimation is larger for the deeper anomaly position (Figure 6b) associated with lower sensitivity. An additional effect caused by the underestimated phase values is the change in the slope of the recovered phase spectrum for different depth positions, which affects the fitting of the CC exponent c (describing the degree of dispersion). This spectral distortion effect is more pronounced for the deeper anomaly position (Figure 6b), associated with regions of lower sensitivity. Intrinsic spectra recovered for the shallower anomaly position exhibit a larger spread within the anomaly (Figure 6a, black curves), indicating a stronger variation of the sensitivities in the anomaly region.

Reconstruction quality of m decreases with decreasing sensitivity (Figure 7a), similar to the behaviour observed for the

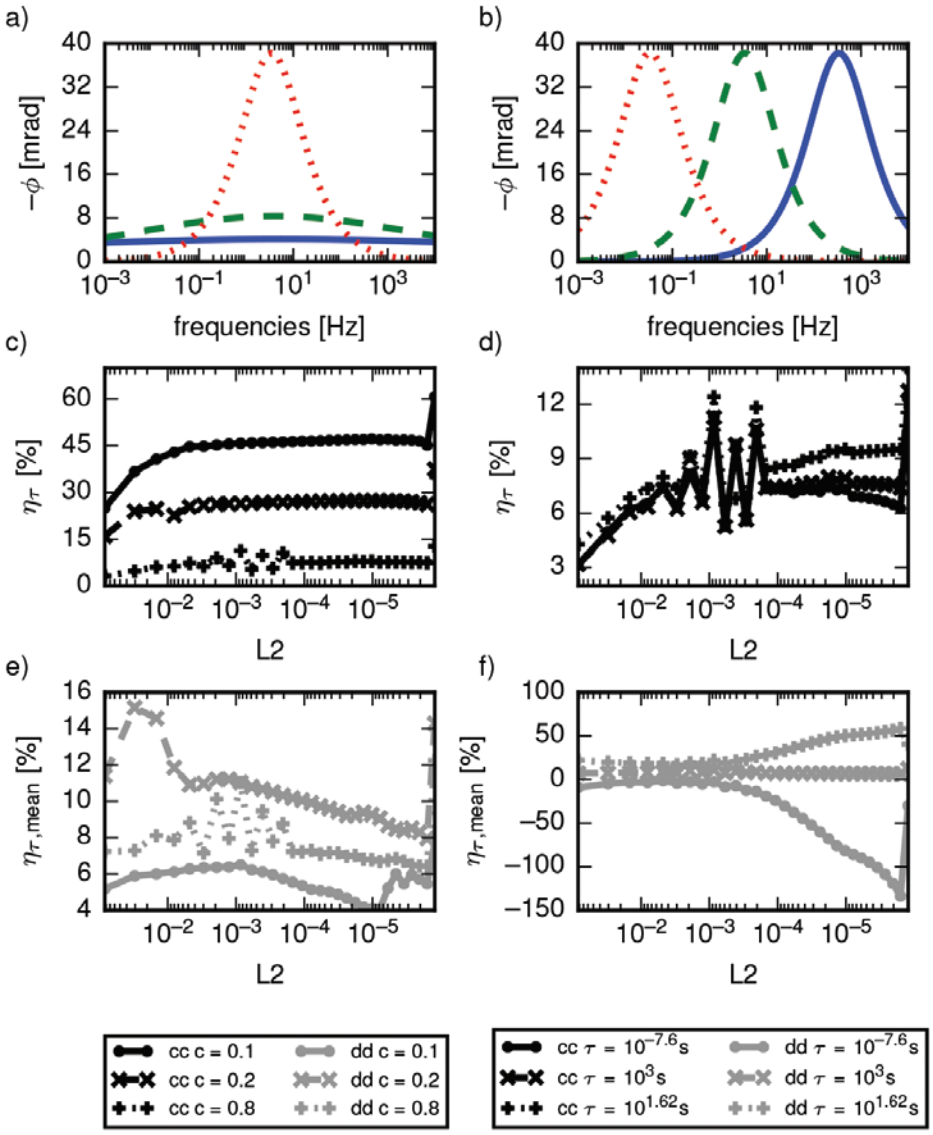

Figure 9 (a) CC model phase responses for different values of c (c = 0.1: blue, c = 0.2: green, c = 0.8: red) with τ = 0.049 s, ρ_0 = 100 Ωm, and m = 0.1. (b) CC model phase responses for different values of τ (τ = 5 s: red, τ = 0.049 s: green, $\tau = 5 \cdot 10^{-4}$ s: blue) with c = 0.8, ρ_0 = 100 Ωm, and m = 0.1. (c–f) Reconstruction quality parameters for the recovered CC and DD relaxation time parameters of the anomaly pixels for different original CC parameter values of c and τ, respectively, plotted against decreasing sensitivity values (L_2), i.e., increasing depth locations of the anomaly. (c and d) η_τ; (e and f) $\eta_{\tau,\mathrm{mean}}$.

reconstruction of the (single-frequency) phase value (cf. Figure 5). The reconstruction curves for m also reveal a dependence relation on the level of noise in the phase data, with larger deviations between recovered and original values for higher noise levels and, thus, lower contrast in the inversion results. The DD parameter m_{tot} (Figure 7b) shows a reconstruction behaviour similar to that of m (Figure 7a).

The reconstruction quality of c shows a dependence relation on sensitivity, but not a monotonic one (Figure 7e). While m and m_{tot} are underestimated over the whole sensitivity range (Figure 7a,b), c reconstruction varies widely and shows smaller deviations for more noisy data and, thus, a lower degree of fitting (Figure 7e).

The reconstruction quality of τ and τ_{mean} differs significantly from that for m, m_{tot}, and c, as the reconstruction quality curves of the relaxation times show no systematic dependence on sensitivity. However, small noise levels of 0.05 mrad lead to some erratic behaviour for low sensitivity values below 10^{-4} (normalised L_2 value), showing variations up to 20% (Figure 7c,d).

If the level of phase data noise is underestimated in the inversion, m and m_{tot} reconstruction curves are shifted to smaller sensitivities, that is, for the same sensitivity (depth), the recovered contrast is slightly increased when noise is underestimated (on the account of overfitting the data) (Figure 8a,b). The reconstruction curves of τ and τ_{mean} become more erratic for increasing underestimation of the data noise level (Figure 8c,d), and also, c reconstruction quality decreases (Figure 8e), especially at low sensitivities. However, reconstructed relaxation time values stay within 60% of the original τ value for a ten-fold underestimation of the actual phase data noise level in the inversion.

The reconstruction quality of CC relaxation time τ decreases for decreasing c values, i.e., decreasing frequency dependence in the spectrum (Figure 9a,c). The corresponding recovered DD relaxation times τ_{mean}, however, stay within 16% of the original τ

values (Figure 9e). For different positions of the phase peak, i.e., different original τ values (Figure 9b), the reconstruction quality of CC relaxation time does vary only within 14% (Figure 9d). The corresponding DD relaxation times τ_{mean} show deviations from the original τ values that increase enormously at lower sensitivities (Figure 9f), which is an effect of the strong dependence of the DD results on the position of the spectral response in the analysed frequency range (Weigand and Kemna 2016b).

DISCUSSION

Reconstruction quality of resistivity and polarisation parameters

To understand the reconstruction behaviour of SIP parameters, it is important to also understand the reconstruction quality of the single-frequency magnitude and phase values. Pelton *et al.* (1978) already noted that parameter m is primarily sensitive to phase angle ϕ, and thus, it is not surprising that the reconstruction curves (i.e., the reconstruction quality as a function of cumulated sensitivity) of m and ϕ are similar in shape (cf. Figures 5e and 7a,b). We explain the loss of reconstruction quality of ϕ (as well as of m and m_{tot}) with the (non-linearly) decreasing signal-to-noise ratio (SNR) with deeper anomaly position (cf. Figure 2b). This effect is well known for DC resistivity imaging. Although the loss of sensitivity and resolution with depth is inherent to the method and thus inevitable, a careful design of the electrode layout and measurement configurations may help mitigate this effect. This also holds for cross-borehole imaging applications, where the loss of sensitivity/resolution is related to the distance to the boreholes. Another factor contributing to the SNR is the given phase contrast of the anomaly relative to the background. An anomaly with a large phase contrast will be better resolved than one with only a weak contrast.

As observed in Figures 7 and 8, data error quantification and its adequate consideration in the inversion play a significant role in the quantitative imaging of CC parameters. The addition of noise to the phase data, or the inversion of the data to an inadequate noise level, affects the reconstruction curve for ϕ (as well as for m and m_{tot}). We explain this as the result of over/underfitting the data in the inversion. While underfitting the data can produce larger contrasts in the inversion results (Figure 8a,b), it also introduces artefacts in the images and amplifies noise components. This comes into effect for the reconstruction of relaxation times (Figure 8c,d).

Reconstruction quality of spectral parameters

Regarding the shape of the spectral response, the c reconstruction curve can be divided into two parts: For high sensitivities, the c values are correctly estimated (or slightly overestimated), and below a certain sensitivity threshold value, they are underestimated (Figure 7e). To understand this pattern, it is necessary to consider the reconstructed phase values in the different regions of the spectrum. As previously discussed, due to variations in the SNR, large (absolute) phase values that form the phase peak will be better reconstructed than smaller (absolute) phase values at the spectral edges of the CC model response (Figure 6). We explain the behaviour observed in Figure 7e as follows: In high-sensitivity regions, the loss of reconstruction quality for the edge values dominates over the loss of reconstruction quality for the peak values (see changing slope of the curve in Figure 5e), resulting in steeper slopes of the recovered spectral response and, thus, an overestimation of c. With decreasing sensitivity, at some point, the loss of reconstruction quality for the peak values will lead to a flattened spectral response with c values smaller than the original ones. This behaviour can be expected, with certain variations due to changing SNR values, for different anomaly parameterisations, phase error estimations, and noise levels. However, as observed in Figure 8e, an underestimation of data noise level leads to an unpredictable reconstruction behaviour of c, possibly due to stronger influence of noise components in inversion. This, in turn, has a direct influence on the slope of the intrinsic spectra and, correspondingly, on parameter c. The reconstruction of the c parameter, and to a certain extent the chargeabilities m and m_{tot}, can possibly be improved by using a frequency regularisation scheme in the inversion (e.g., Kemna *et al.* 2014; Günther and Martin 2016): If a smoothness of suitable strength is imposed on the spectrum, then its original form can be retained over a larger SNR bandwidth, i.e., down to larger depths.

The reconstruction quality of the CC relaxation time τ and the DD relaxation time τ_{mean} differ significantly from the results for ρ_0, m, m_{tot}, and c, revealing a stable, i.e., sensitivity-independent, reconstruction quality over a large range of sensitivity values. This can be explained by the direct relation of τ to the frequency position of the phase peak, which is more robust to data noise, error underestimation, and small sensitivities than the other features of the spectral CR response used to determine ρ_0, m, m_{tot}, and c. The relaxation time is (inversely) proportional to the peak frequency, i.e., the frequency at which the strongest polarisation response is observed (e.g., Pelton *et al.* 1978). Hence, this parameter is only dependent on the position of the peak in the spectrum, but not on the resistivity or phase values. Therefore, under/overfitting in the inversion should not impact the reconstruction quality of τ and τ_{mean}, as long as the peak in the spectrum is not strongly distorted (cf. Figure 6). Furthermore, the interpretation of τ and τ_{mean} results will not be influenced (to a certain degree) by the varying image resolution or different noise levels, as would be the other parameters (cf. Figure 7). This result is extremely important for SIP imaging applications as it implies that the recovered relaxation time values will be less dependent on the electrode configuration of the survey and of similar quality over a large sensitivity (and thus image) region. Merely the underestimation of data noise has a larger effect on recovered relaxation times (Figure 8c,d). However, the observed 60% deviation is still relatively small compared with the overall dynamics of multiple magnitudes that can be observed for relaxation times (e.g., Pelton *et al.* 1978).

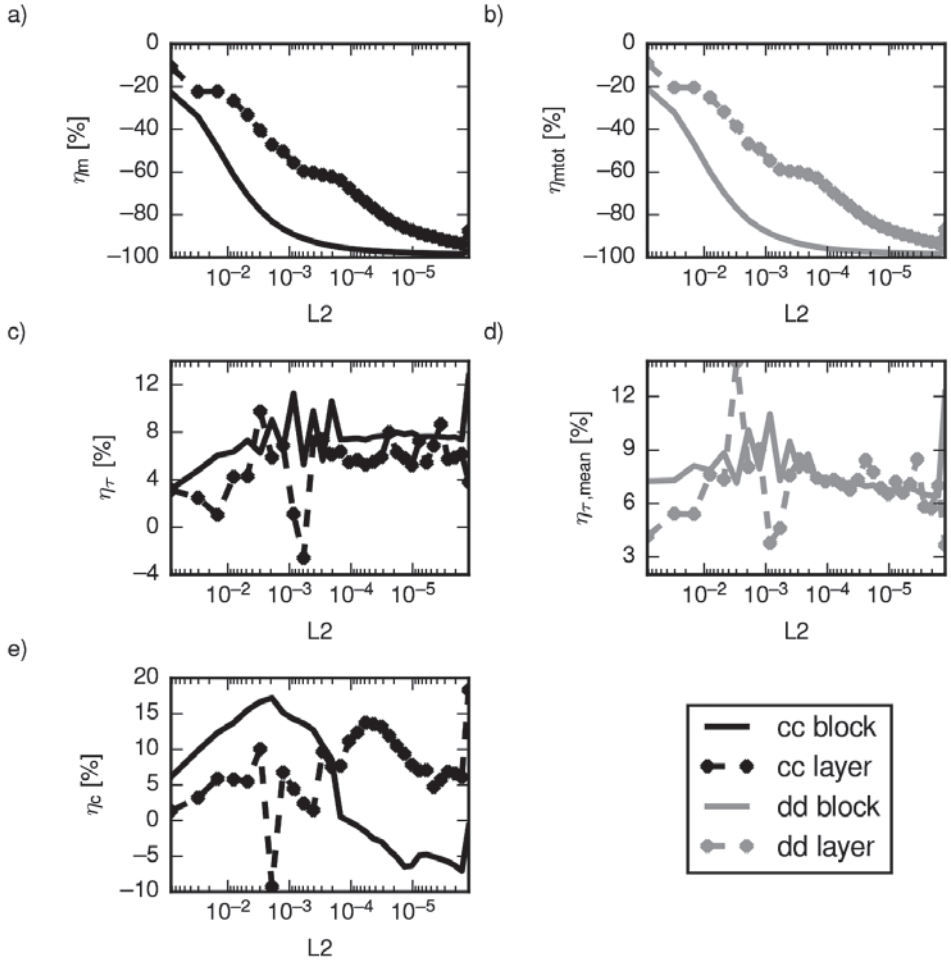

Figure 10 Reconstruction quality parameters for the recovered CC and DD parameters of the anomaly pixels plotted against decreasing sensitivity values (L_2), i.e., increasing depth locations of the anomaly. (a) $\eta_{\mathbf{m}}$, (b) $\eta_{\mathbf{mtot}}$, (c) η_{τ}, (d) $\eta_{\tau,\mathbf{mean}}$, (e) $\eta_{\mathbf{c}}$. Results for a block anomaly (block; cf. Figure 8) and a layered anomaly (layer) are compared. Simulations were performed for a phase data noise level of 0.5 mrad and a corresponding error estimate in the inversion.

Quantitative imaging of CC parameters may play a significant role in the characterisation of processes relevant in hydrogeological and environmental studies. However, petrophysical relationships are still required to derive information of interest from CC/DD parameters. For instance, recent studies have demonstrated a strong correlation between hydraulic conductivity (or permeability), governing groundwater flow, and the length scale at which the polarisation takes place, i.e., a characteristic relaxation time τ (e.g., Binley *et al.* 2005; Revil and Florsch 2010; Zisser, Kemna and Nover 2010). However, several works have also investigated the link between a single-frequency CR parameter and important textural properties, such as surface-area-to-pore-volume ratio (e.g., Börner, Schopper and Weller 1996; Slater and Lesmes 2002; Weller *et al.* 2010), which could also be used to estimate hydraulic conductivity. While both single-frequency and multi-frequency CR imaging may thus be used to estimate the same parameter (e.g., hydraulic conductivity), the results presented in our study suggest that, for imaging surveys, petrophysical relationships relying on relaxation times (τ, τ_{mean}) are better suited than those based on m, m_{tot}, or ϕ, given the better reconstruction quality of τ. We have shown that the τ reconstruction quality is robust with respect to different noise levels in the data; however, it is important that the considered frequency range is wide enough to capture the spectral behaviour. Hence, we also conclude that the quality of the reconstruction will benefit from the acquisition of broadband CR measurements, preferably with dense spectral sampling.

Application to more complex scenarios

In this study, we consider a simple model of a polarisable anomaly with a CC model response in a homogeneous, unpolarisable background. This setting is transferable to only a limited number of real-life scenarios. For example, certain tracer tests could provide a situation in which the results of this study can be directly applied. In general, the subsurface will exhibit a more complex, heterogeneous structure, and other aspects, such as shielding effects of high-resistive layers, will become important. Furthermore, with increasing inhomogeneity of a given subsurface resistivity distribution, regularisation effects will influence inversion results to a much larger degree. Analysing such scenarios would greatly overreach this study and is left for future studies. However, as a preview on possible research directions, Figure 10 shows the reconstruction curves

of CC and DD parameters for a setting similar to the one presented in Figure 7. Data noise with a standard deviation of 0.5 mrad is added to the data, and the corresponding error estimates are used in the inversion. Intrinsic spectra are extracted from 2 m × 2 m areas successively moved to deeper locations, as is done in the previous simulations. However, instead of considering a local anomalous block, the whole depth layer is parameterised with a given CC model response. Thus, a simple layered structure is simulated, as for example found when sedimentary layers are investigated. Intrinsic spectra are only extracted from the center of the modelling grid to exclude boundary effects of the regularisation. The reconstruction of m and m_{tot} is greatly improved over the non-layered case (Figure 10a,b), while relaxation times do not show large variations (below 10%) from each other (Figure 10c,d). Merely c reconstruction shows differences in its reconstruction behaviour (Figure 10e), whose origin is not yet clear and must be addressed in future work.

We believe that our results on the reconstruction quality of CC and DD parameters as a function of sensitivity are still applicable to more heterogeneous situations, at least if the given spectral signatures are close to the CC type. Hence, considering our results, we can also suggest that sensitivity values can be used to assess the reliability of the reconstructed parameters in single- and multi-frequency CR imaging. Our results also show that (cumulated) sensitivity can be a sufficient parameter to address reconstruction quality, compared with other computationally more expensive approaches based on a resolution matrix.

CONCLUSIONS

We investigated the reconstruction quality of CC model and DD parameters based on multi-frequency CR imaging by means of numerical simulations. Our results show that the reconstruction quality of CC parameters m and c, as well as of DD parameter m_{tot}, vary strongly across the imaging plane, with reconstructed values deviating considerably from the original values for lower sensitivities. The reconstruction quality of m and m_{tot} decreases monotonically with decreasing sensitivity, while c shows inconclusive behaviour that cannot be explained yet for all scenarios. The same dependence in the reconstruction quality curves is observed for the diagonal entries of the model resolution matrix. Therefore, based on our results, cumulated sensitivity (regardless of whether its L_1 or its L_2 measure is used) appears to be an adequate, computationally inexpensive proxy for image resolution. Opposite to this, the reconstruction quality of CC relaxation time τ and DD relaxation time τ_{mean} is only weakly dependent on sensitivity, resulting in fair quantitative reconstructions even in regions with relatively low sensitivity (deviation less than 20% from the original value down to normalised L_2 cumulated sensitivity values of 10^{-4}).

Our results suggest that a quantitative interpretation of relaxation time parameters (either from CC model fit or DD), and any parameters derived from them using established petrophysical relationships, is also possible in a multi-frequency CR imaging framework. The recovery of chargeabilities m or m_{tot}, as well as the CC exponent c, on the other hand, is highly affected by the imaging characteristics (sensitivity, resolution), which must be carefully taken into account if a quantitative interpretation is intended. Given the strong correlation between CC model parameters (and corresponding DD parameters) and various petrophysical properties of relevance in hydrogeological and environmental applications, as demonstrated by a large number of studies over the last years, our findings are of outermost importance for the successful quantitative application of multi-frequency CR imaging for improved subsurface characterisation.

ACKNOWLEDGEMENTS

Parts of this work were conducted in the framework of the SFB TR32 “Patterns in soil-vegetation-atmosphere systems: monitoring, modeling and data assimilation” funded by the Deutsche Forschungsgemeinschaft (DFG). The authors would like to thank the two anonymous referees for their very constructive reviews.

REFERENCES

Abdel Aal G.Z., Atekwana E.A., Slater L.D. and Atekwana E.A. 2004. Effects of microbial processes on electrolytic and interfacial electrical properties of unconsolidated sediments. *Geophysical Research Letters* **31**(12).

Alumbaugh D.L. and Newman G.A. 2000. Image appraisal for 2-D and 3-D electromagnetic inversion. *Geophysics* **65**(5), 1455–1467.

Atekwana E.A. and Slater L.D. 2009. Biogeophysics: a new frontier in earth science research. *Reviews of Geophysics* **47**(4).

Binley A. and Kemna A. 2005. DC resistivity and induced polarization methods. In: *Hydrogeophysics* (eds Y. Rubin and S. Hubbard), pp. 129–156. Netherlands: Springer.

Binley A., Slater L.D., Fukes M. and Cassiani G. 2005. Relationship between spectral induced polarization and hydraulic properties of saturated and unsaturated sandstone. *Water Resources Research* **41**(12), 1–13.

Börner F.D., Schopper J.R. and Weller A. 1996. Evaluation of transport and storage properties in the soil and groundwater zone from induced polarization measurements. *Geophysical Prospecting* **44**(4), 583–601.

Cole K.S. and Cole R.H. 1941. Dispersion and absorption in dielectrics I. Alternating current characteristics. *Journal of Chemical Physics* **9**(4), 341–351.

Davis C.A., Atekwana E., Atekwana E., Slater L.D., Rossbach S. and Mormile M.R. 2006. Microbial growth and biofilm formation in geologic media is detected with complex conductivity measurements. *Geophysical Research Letters* **33**(18).

Day-Lewis F.D., Singha K. and Binley A.M. 2005. Applying petrophysical models to radar travel time and electrical resistivity tomograms: resolution-dependent limitations. *Journal of Geophysical Research* **110**(B8).

Flores Orozco A., Williams K.H., Long P.E., Hubbard S.S. and Kemna A. 2011. Using complex resistivity imaging to infer biogeochemical processes associated with bioremediation of an uranium-contaminated aquifer. *Journal of Geophysical Research* **116**(G3).

Flores Orozco A., Kemna A., Oberdörster C., Zschornack L., Leven C., Dietrich P. *et al.* 2012a. Delineation of subsurface hydrocarbon contamination at a former hydrogenation plant using spectral induced polarization imaging. *Journal of Contaminant Hydrology* **136**, 131–144.

Flores Orozco A., Kemna A. and Zimmermann E. 2012b. Data error quantification in spectral induced polarization imaging. *Geophysics* **77**(3), E227–E237.

Flores Orozco A., Williams K.H. and Kemna A. 2013. Time-lapse spectral induced polarization imaging of stimulated uranium bioremediation. *Near Surface Geophysics* **11**(5), 531–544.

Flores Orozco A., Velimirovic M., Tosco T., Kemna A., Sapion H., Klaas N. *et al.* 2015. Monitoring the injection of microscale zerovalent iron particles for groundwater remediation by means of complex electrical conductivity imaging. *Environmental Science & Technology* **49**(9), 5593–5600.

Florsch N., Revil A. and Camerlynck C. 2014. Inversion of generalized relaxation time distributions with optimized damping parameter. *Journal of Applied Geophysics* **109**, 119–132.

Friedel S. 2003. Resolution, stability and efficiency of resistivity tomography estimated from a generalized inverse approach. *Geophysical Journal International* **153**(2), 305–316.

Günther T. and Martin T. 2016. Spectral two-dimensional inversion of frequency-domain induced polarization data from a mining slag heap. *Journal of Applied Geophysics* **135**, 436-448.

Hördt A., Blaschek R., Kemna A. and Zisser N. 2007. Hydraulic conductivity estimation from induced polarisation data at the field scale—the Krauthausen case history. *Journal of Applied Geophysics* **62**(1), 33–46.

Kemna A. 2000. *Tomographic inversion of complex resistivity—theory and application*. PhD thesis, Ruhr-Universität Bochum, Germany.

Kemna A., Vanderborght J., Kulessa B., and Vereecken H. 2002. Imaging and characterisation of subsurface solute transport using electrical resistivity tomography (ERT) and equivalent transport models, *Journal of Hydrology* **267**, 125–146.

Kemna A., Binley A. and Slater L. 2004. Crosshole IP imaging for engineering and environmental applications. *Geophysics* **69**(1), 97–107.

Kemna A., Binley A., Cassiani G., Niederleithinger E., Revil A., Slater L. *et al.* 2012. An overview of the spectral induced polarization method for near-surface applications. *Near Surface Geophysics* **10**(6), 453–468.

Kemna A., Huisman J.A., Zimmermann E., Martin R., Zhao Y., Treichel A. *et al.* 2014. Broadband electrical impedance tomography for subsurface characterization using improved corrections of electromagnetic coupling and spectral regularization. In: *Tomography of the Earth's Crust: From Geophysical Sounding to Real-Time Monitoring*, pp. 1–20. Springer.

Lesmes D.P. and Morgan F.D. 2001. Dielectric spectroscopy of sedimentary rocks. *Journal of Geophysical Research* **106**(B7), 13329–13346.

Luo Y. and Zhang G. 1998. *Theory and Application of Spectral Induced Polarization*. Tulsa: Society of Exploration Geophysicists.

Mwakanyamale K., Slater L., Binley A. and Ntarlagiannis D. 2012. Lithologic imaging using complex conductivity: lessons learned from the Hanford 300 Area. *Geophysics* **77**(6), E397–E409.

Nguyen F., Kemna A., Antonsson A., Engesgaard P., Kuras O., Ogilvy R. *et al.* 2009. Characterization of seawater intrusion using 2D electrical imaging. *Near Surface Geophysics* **7**(5-6), 377– 390.

Nordsiek S. and Weller A. 2008. A new approach to fitting induced-polarization spectra. *Geophysics* **73**(6), F235–F245.

Ntarlagiannis D., Williams K.H., Slater L. and Hubbard S. 2005. Low-frequency electrical response to microbial induced sulfide precipitation. *Journal of Geophysical Research* **110**(G02009).

Oldenburg D.W. and Li Y. 1999. Estimating depth of investigation in DC resistivity and IP surveys. *Geophysics* **64**(2), 403–416.

Pelton W.H., Ward S.H., Hallof P.G., Sill W.R. and Nelson P.H. 1978. Mineral discrimination and removal of inductive coupling with multifrequency IP. *Geophysics* **43**(3), 588–609.

Revil A. and Florsch N. 2010. Determination of permeability from spectral induced polarization in granular media. *Geophysical Journal International* **181**(3), 1480–1498.

Slater L. 2007. Near surface electrical characterization of hydraulic conductivity: from petrophysical properties to aquifer geometries—a review. *Surveys in Geophysics* **28**(2-3), 169–197.

Slater L. and Lesmes D.P. 2002. Electrical-hydraulic relationships observed for unconsolidated sediments. *Water Resources Research* **38**(10), 31-1 – 31-13.

Slater L. and Binley A. 2006. Synthetic and field-based electrical imaging of a zerovalent iron barrier: implications for monitoring long-term barrier performance. *Geophysics* **71**(5), B129–B137.

Vanhala H. 1997. Mapping oil-contaminated sand and till with the spectral induced polarization (SIP) method. *Geophysical Prospecting* **45**(2), 303–326.

Weigand M. and Kemna A. 2016a. Multi-frequency electrical impedance tomography as a non-invasive tool to characterize and monitor crop root systems. *Biogeosciences Discussions* 2016, 1–31. *http://www.biogeosciences-discuss.net/bg-2016-154/.*

Weigand M. and Kemna A. 2016b. Debye decomposition of time-lapse spectral induced polarisation data. *Computers and Geosciences* **86**, 34–45.

Weigand M. and Kemna A. 2016c. Relationship between Cole–Cole model parameters and spectral decomposition parameters derived from SIP data. *Geophysical Journal International* **205**, 1414–1419.

Weller A., Slater L., Nordsiek S. and Ntarlagiannis D. 2010. On the estimation of specific surface per unit pore volume from induced polarization: a robust empirical relation fits multiple data sets. *Geophysics* **75**(4), WA105–WA112.

Williams K.H., Kemna A., Wilkins M.J., Druhan J., Arntzen E., N'Guessan A.L. *et al.* 2009. Geophysical monitoring of coupled microbial and geochemical processes during stimulated subsurface bioremediation. *Environmental Science & Technology* **43**(17), 6717–6723.

Zanetti C., Weller A., Vennetier M. and Mériaux P. 2011. Detection of buried tree root samples by using geoelectrical measurements: a laboratory experiment. *Plant and Soil* **339**(1-2), 273–283.

Zisser N., Kemna A. and Nover G. 2010. Relationship between low-frequency electrical properties and hydraulic permeability of low-permeability sandstones. *Geophysics* **75**(3), E131–E141.

APPENDIX

A. Complex resistivity inversion

CR images are computed using the inversion code of Kemna (2000). The code computes the distribution of CR ρ (expressed in magnitude ($|\rho|$) and phase (ϕ)), in a 2D (x, z) image plane from a given dataset of complex transfer impedances Z_i (expressed in magnitude ($|Z_i|$) and phase (ϕ_i)) under the constraint of maximum smoothness. The algorithm iteratively minimises a cost function $\Psi(\underline{m})$, which is composed of the measures of data misfit and model roughness, with both terms being balanced by a (real-valued) regularisation parameter λ:

$$\Psi(\underline{m}) = \left\| \underline{\underline{W}}_{\mathrm{d}} \left(\underline{d} - \underline{f}(\underline{m}) \right) \right\|^2 + \lambda \left\| \underline{\underline{W}}_{\mathrm{m}} \underline{m} \right\|^2, \quad (8)$$

where $\underline{d}$ is the data vector (log impedance data), $\underline{m}$ is the model parameter vector (log complex resistivities of parameter cells (lumped elements of underlying finite-element mesh)), $\underline{f}(\underline{m})$is the operator of the forward model, $\underline{\underline{W}}_{\mathrm{d}}$ is a data weighting matrix,

and $\underline{\underline{W}}_{\mathrm{m}}$ is a (real-valued) matrix evaluating the first-order roughness of $\underline{m}$. Under the assumption that the data errors are uncorrelated and normally distributed, $\underline{\underline{W}}_{\mathrm{d}}$ is a diagonal matrix given by

$$\underline{\underline{W}}_{\mathrm{d}} = \begin{pmatrix} \frac{1}{\epsilon_1} & 0 & 0 \\ 0 & \ddots & 0 \\ 0 & 0 & \frac{1}{\epsilon_n} \end{pmatrix}, \tag{9}$$

where ϵ_i is the complex error estimate (standard deviation) of the ith datum, i.e., $d_i = \ln(Z_i) + j\phi_i$ (with j denoting the imaginary unit). At each iteration step of the inversion, a univariate search is performed to find the maximum value of the regularisation parameter λ that locally minimises the data misfit.

In CR inversion, the data misfit is typically dominated by the real component of the complex data (that is log impedance magnitude). To properly take into account the misfit in the phase (imaginary component of the data), subsequent to the complex inversion, additional inversion iterations are run only for the phase (i.e., as a real-valued inverse problem with the impedance phase values as data and the CR phase values as parameters). Here, the resistivity magnitude image from the complex inversion is kept unchanged, and the same smoothness-constrained inversion procedure is used. For more details on the implementation of the inversion, we refer to Kemna (2000).

B. Image appraisal

Electrical resistivity images exhibit a variable spatial resolution (e.g., Oldenburg and Li 1999; Friedel 2003; Binley and Kemna 2005). A common approach for the quantification of this variable resolution uses the diagonal entries of the model resolution matrix, $\underline{\underline{R}}$ (e.g., Alumbaugh and Newman 2000), which, for the complex case, is given by

$$\underline{\underline{R}} = \left[\underline{\underline{A}}^H \underline{\underline{W}}_{\mathrm{d}}{}^H \underline{\underline{W}}_{\mathrm{d}} \underline{\underline{A}} + \lambda \underline{\underline{W}}_{\mathrm{m}}{}^T \underline{\underline{W}}_{\mathrm{m}} \right]^{-1} \left[\underline{\underline{A}}^H \underline{\underline{W}}_{\mathrm{d}}{}^H \underline{\underline{W}}_{\mathrm{d}} \underline{\underline{A}} \right], \tag{10}$$

where $\underline{\underline{A}} = \frac{\partial \underline{f}(\underline{m})}{\partial \underline{m}}$ is the complex Jacobian matrix (for its computation, see Kemna (2000)). The model resolution matrix is usually evaluated at the end of the iterative inversion process. Due to its lower computational cost compared with $\underline{\underline{R}}$, the cumulative (and error-weighted) sensitivity, $\underline{s}_{\mathrm{L2}}$, has been alternatively used (e.g., Kemna *et al.* 2002; Nguyen *et al.* 2009). Using the L_2-norm, its components are given by Kemna (2000) as

$$(\underline{s}_{\mathrm{L2}})_k = \mathrm{diag}\left(\underline{\underline{A}}^H \underline{\underline{W}}_d{}^H \underline{\underline{W}}_d \underline{\underline{A}} \right) = \sum_i \frac{|a_{ik}|^2}{|\epsilon_i|^2}, \tag{11}$$

where a_{ik} is the i,kth element of the Jacobian matrix $\underline{\underline{A}}$, i.e., the sensitivity of the ith datum with respect to the kth parameter cell. Note that also for the complex case, $\underline{s}_{\mathrm{L2}}$ is a real-valued vector. The cumulated sensitivity is a measure of how much an entire dataset changes due to a changing model cell. Given the correspondence between cumulated sensitivity and the diagonal of the model resolution matrix, the cumulated sensitivity can be used as a proxy for model resolution. We emphasise here that a large cumulated sensitivity does not necessarily imply a good resolution; however, good resolution cannot be expected for model cells exhibiting small cumulative sensitivities (Kemna 2000).

In addition to the L_2-normed cumulated sensitivity, in our study, we also compute the L_1-normed cumulated sensitivity based on the sum of the absolute values of the sensitivities (weighted by the absolute error of the corresponding measurement):

$$(\underline{s}_{\mathrm{L1}})_k = \sum_i \frac{|a_{ik}|}{|\epsilon_i|}. \tag{12}$$